JOURNAL OF AIRCRAFT
Vol. 36, No. 2, March–April 1999

Hopf-Bifurcation Analysis of Airfoil Flutter at Transonic Speeds

Scott A. Morton* and Philip S. Beran†
U.S. Air Force Institute of Technology, Wright–Patterson Air Force Base, Ohio 45433-7542

Hopf-bifurcation analysis is used to determine flutter onset for a pitch-and-plunge airfoil at transonic Mach number conditions. The pitch-and-plunge model is a coupling of the Euler equations and a two-degree-of-freedom structural model composed of linear and torsional springs. The Euler equations are discretized using the upwind total variation diminishing scheme of Harten and Yee. Equilibrium solutions of the aeroelastic model are computed using Newton's method, and dynamic solutions are explicitly integrated in time with first-order accuracy. The Hopf-bifurcation point, which models the flutter condition, is computed directly using a modified form of the Griewank and Reddien algorithm. A path of Hopf points is computed as a function of Mach number to produce a Mach flutter boundary. The flutter boundary is validated by time integration. Flutter boundaries are also obtained through variation of static pretwist and pitch and plunge damping. The direct, Hopf-point method is found to be precise and efficient for grids typical of inviscid, transonic airfoil calculations.

Nomenclature

b, c = airfoil half-chord and chord
C_l, C_m = airfoil section lift and moment coefficients
$\hat{e}_1$, $\hat{e}_2$ = unit vectors in airfoil-fixed reference system
$\boldsymbol{G}$ = nonlinear fluid–structure interaction system
h = vertical displacement (positive up)
I_α = pitch axis moment of inertia
$\hat{i}$, $\hat{j}$ = unit vectors in inertial axis
J = Jacobian of coordinate transformation
m = airfoil mass per unit span
t, T = time, period of limit cycle oscillation
$\bar{u}$ = reduced velocity, $V_\infty/(b\omega_\alpha)$
u, v = velocity components in airfoil-fixed reference system
u_g, v_g = grid speeds
V_∞ = freestream velocity
x, y = coordinates in airfoil-fixed reference system
$\boldsymbol{Y}$ = fluid–structure interaction dependent variable
α, α_0 = geometric angle of attack and static pretwist, deg
ζ_α, ζ_h = pitch and vertical axes structural damping ratios
Θ = critical eigenvalue imaginary part
$\tilde{\lambda}$ = free parameter of the fluid–structure system
ξ, η = transformed coordinates tangent and normal to airfoil surface
ω_α, ω_h = pitch and vertical axes natural frequency, $\sqrt{K_\alpha/I_\alpha}$ and $\sqrt{K_h/m}$

Subscripts

ea = referenced to elastic axis
i, j = location of grid point
in = in inertial reference frame
∞ = freestream quantity

Introduction

AEROELASTICITY has been an area of research interest for many years. Of particular interest is the aeroelastic phenomenon called flutter, which is an oscillatory aerodynamic condition resulting from fluid–structure interaction. The instability can be associated with the formation of large vortical structures, as in the case of the low-speed, high angle-of-attack flow regime or associated with complex shock-wave motion in the transonic regime. The high-frequency and large-amplitude motion that results from flutter can cause a loss of structural integrity in wings. For this reason, the prediction of flutter is of the utmost importance.

Edwards and Thomas[1] and Edwards and Malone[2] have written summary papers on the transonic aeroelasticity problem. In these papers they discuss the various types of oscillatory flow, the various mathematical models necessary to simulate the phenomenon, and a list of experimental data to be used for comparison. Reference 1 primarily discusses two-dimensional modeling and experiments, whereas Ref. 2 focuses on the three-dimensional problem. Wu et al.[3] and Kousen and Bendiksen[4] analyzed the transonic airfoil at conditions similar to the current study.

Time integration has been the primary method of determining the flutter point in numerical experiments. Some investigators have taken an alternate approach of calculating the flutter point by computing the Hopf-bifurcation point and then inferring a crossing of the flutter point. Hui and Tobak[5] used bifurcation analysis to determine a flutter point for simplified aerodynamic and structural models, solving for the flow over flat-plate airfoils at supersonic and hypersonic speeds with single-degree-of-freedom pitching motion. The work of Beran and Lutton[6] developed the direct method for the incompressible stream-function-vorticity formulation of the Navier–Stokes equations for a static airfoil. Morton and Beran[7] analyzed the eigenvalue behavior of a NACA 64A006 pitch-and-plunge airfoil (PAPA) in inviscid flow, and observe the crossing of a flutter point with changes in reduced velocity. They validate the implied change in stability properties through time integration. Morton and Beran[8] and Morton[9] report results of a method for the direct computation of the critical reduced velocity at which flutter begins.

Airfoil flutter at transonic speeds involves complex shock-wave structures and their interaction with a dynamic body. In the current investigation, Hopf-bifurcation analysis is used to

---

Received June 9, 1996; revision received March 30, 1998; accepted for publication June 12, 1998.

*Major, USAF, Computational Aerodynamicist; currently Assistant Professor, Aeronautics Department, HQ USAFA/DFAN, 2354 Fairchild Drive, Suite 6H22, U.S. Air Force Academy, CO 80840-6222. Senior Member AIAA.

†Associate Professor, 2950 P. Street, Building 640. Senior Member AIAA.

locate the flutter onset point for flow over an airfoil with pitch-and-plunge freedom at transonic conditions. The approach outlined in Refs. 8 and 9 is used, whereby the dynamic motion of the airfoil is modeled through a two-degree-of-freedom, PAPA model consisting of linear and torsional springs. A total variation diminishing (TVD) scheme is used to discretize the Euler equations in strong-conservation law form.[10] This approach can accurately model airfoils with large-amplitude motions at transonic freestream Mach numbers.[10]

The system of nonlinear equations resulting from spatial discretization of the governing equations is expressed as

$$\boldsymbol{Y}_t = \boldsymbol{G}(\boldsymbol{Y}, \tilde{\lambda}) \tag{1}$$

where $\boldsymbol{Y}$ is the solution vector, $\tilde{\lambda}$ is a parameter of the system, and G is the spatial discretization of the nonlinear system. Equilibrium solutions satisfy

$$\boldsymbol{G}(\boldsymbol{Y}, \tilde{\lambda}) = 0 \tag{2}$$

The points that comprise solution paths can be classified as solutions to the time-independent equations or solutions to the time-dependent equations. The Jacobian matrix, $\boldsymbol{G}_Y$, of the equilibrium system [Eq. (2)] has a set of eigenvalues, $\{\beta_j\}$. Evaluated at an equilibrium solution, the real parts of β_j determine linear system stability.[11] If the real part of β_j is less than zero for all j, the equilibrium point is stable to infinitesimal perturbations. If the real part of β_j is greater than zero for one or more j, the point is unstable, resulting in time-dependent behavior of the system. Seydel[11] states that if at a point defined by the pair $(\boldsymbol{Y}^*, \tilde{\lambda}^*)$, three conditions hold, then from the point emerges a branch of unsteady solutions with limit-cycle behavior. This singular point is called a Hopf-bifurcation point, and the three Hopf-point conditions are 1) the steady-state equations are satisfied, $\boldsymbol{G}(\boldsymbol{Y}^*, \tilde{\lambda}^*) = 0$; 2) the Jacobian matrix $\boldsymbol{G}_Y^* \equiv \boldsymbol{G}_Y(\boldsymbol{Y}^*, \tilde{\lambda}^*)$ has a pair of purely imaginary eigenvalues (with no other eigenvalue having vanishing real part): $\beta_\pm = \pm i\Theta$ $(\Theta \neq 0)$; and 3) the transversality condition is satisfied: $(d/d\tilde{\lambda})(\text{Real}[\beta_\pm(\tilde{\lambda})])|_{\tilde{\lambda}=\tilde{\lambda}^*} \neq 0$. If these conditions are satisfied and there are no other eigenvalue pairs with positive real parts, the Hopf-point is a point of the stability exchange.

Nonlinear analysis of the PAPA solution space is accomplished to study flutter onset. The equations considered expand upon Eq. (2) to include the Hopf-point conditions. By combining the Harten-Yee TVD scheme with a new Hopf-bifurcation algorithm based on the Griewank and Reddien method, the precise location of the Hopf-point, $\tilde{\lambda}^*$, can be determined. The Hopf-point is validated with time integration of the time-dependent equations. Paths of Hopf-points are computed to form stability boundaries by varying relevant physical parameters.

The specific contributions of this work are improved precision and efficiency in computing flutter boundaries of PAPA models for a variety of free parameters. The flutter onset point is computed directly with a high degree of precision, whereas time-integration algorithms have a difficult time in precisely defining flutter onset caused by the region of light damping surrounding the flutter point. Efficiency is gained in two ways. A single flutter point is computed more efficiently by eliminating bracketing of the stability point. Time-integration methods integrate a solution to either a steady state or a stable limit cycle to determine if a flutter point has been crossed. Bracketing a single flutter point may take several time-integration solutions, each consisting of thousands of implicit iterations or hundreds of thousands of explicit iterations. Efficiency is also gained by greatly reducing the number of iterations required to achieve a converged solution, even while the order of computational work per iteration is increased.

Analysis

The equations of motion and the method of solution are presented in this section. Included are the modifications to the Euler equations for a translating and rotating airfoil, the form of the TVD flux formulations, implementation of numerical algorithms for the calculation of unsteady and equilibrium solutions, and the procedure for computing the flutter point.

Equations of Motion

The PAPA model is depicted in Fig. 1. Two reference frames are defined: an inertial reference system $(\hat{\imath}, \hat{\jmath})$ and an airfoil-fixed reference system $(\hat{e}_1, \hat{e}_2)$. It is assumed that the airfoil is constrained to move along the vertical inertial axis and to rotate about an elastic axis.

The governing equations for the two-degree-of-freedom model[4] are presented in nondimensional form and have the following scales:

$$h^* = \frac{h}{c}, \qquad x_\alpha = \frac{r}{b}, \qquad t^* = t\,\frac{V_\infty}{c}, \qquad \bar{u} = \frac{V_\infty}{b\omega_\alpha} \tag{3}$$

$$u^* = \frac{u}{V_\infty}, \qquad v^* = \frac{v}{V_\infty}, \qquad p^* = \frac{p}{\rho_\infty V_\infty^2} \tag{4}$$

where r is the distance from the elastic axis to the c.g., positive forward, and ρ_∞ is the freestream density. Hereafter, the superscript $*$ is dropped for notational convenience, and all variables are understood to be nondimensional. The structural equations in pitch and plunge are as follows:

$$\ddot{h} + \frac{x_\alpha}{2}\,\ddot{\alpha} + 2\zeta_h c_2 \dot{h} + c_2^2 h = \frac{2}{\mu_s \pi}\, C_l \tag{5}$$

$$x_\alpha \ddot{h} + \frac{r_\alpha^2}{2}\,\ddot{\alpha} + \frac{2\zeta_\alpha r_\alpha^2}{\bar{u}}\,\dot{\alpha} + c_1(\alpha - \alpha_0) = \frac{4}{\mu_s \pi}\, C_{m_{\text{ea}}} \tag{6}$$

$$c_1 = \frac{1}{2}\left(\frac{2}{\bar{u}}\right)^2 r_\alpha^2, \qquad c_2 = \left(\frac{2}{\bar{u}}\right)\left(\frac{\omega_h}{\omega_\alpha}\right) \tag{7}$$

where α is measured from the freestream velocity vector to the airfoil chord. The linear and torsional springs are modeled with stiffness coefficients, K_h and K_α, and damping coefficients, D_h and D_α. The static pretwist, α_0, defines the unloaded position of the torsional spring and models a nonvanishing angle of attack at the wing root.

The radius of gyration is $r_\alpha \equiv \sqrt{I_\alpha/m}$. The three remaining parameters are the mass ratio, μ_s, and the damping ratios:

$$\mu_s \equiv \frac{m}{\pi \rho_\infty b^2}, \qquad \zeta_\alpha \equiv \frac{D_\alpha}{2\sqrt{I_\alpha K_\alpha}}, \qquad \zeta_h = \frac{D_h}{2\sqrt{m K_h}}$$

Equations (5) and (6) are rewritten as a system of first-order differential equations by setting $y_1 = h$, $y_3 = \alpha$, $\dot{y}_1 = y_2$ and $\dot{y}_3$

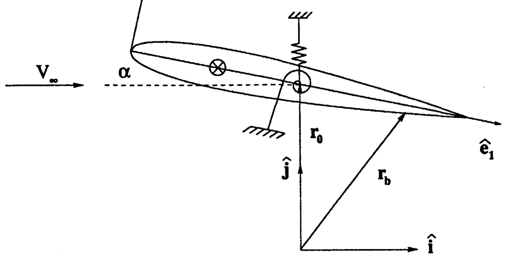

Fig. 1 Inertial and airfoil-fixed reference frames.

$= y_4$. Following the approach of Ref. 9, with det $\equiv \frac{1}{2}(r_\alpha^2 - x_\alpha^2)$, we find

$$S_t = \mathcal{K}(S, C_l, C_{m_{\mathrm{ea}}}, \bar{u}) \tag{8}$$

$$\mathcal{K} \equiv M^{-1}Q - M^{-1}KS \tag{9}$$

$$S \equiv \begin{bmatrix} y_1 \\ y_2 \\ y_3 \\ y_4 \end{bmatrix}, \quad M \equiv \begin{bmatrix} 1 & 0 & 0 & 0 \\ 0 & 1 & 0 & \frac{1}{2}x_\alpha \\ 0 & 0 & 1 & 0 \\ 0 & x_\alpha & 0 & \frac{1}{2}r_\alpha^2 \end{bmatrix}$$

$$M^{-1} = \frac{1}{\det}\begin{bmatrix} \det & 0 & 0 & 0 \\ 0 & \frac{1}{2}r_\alpha^2 & 0 & -\frac{1}{2}x_\alpha \\ 0 & 0 & \det & 0 \\ 0 & -x_\alpha & 0 & 1 \end{bmatrix} \tag{10}$$

$$Q = \begin{bmatrix} 0 \\ \dfrac{2}{\mu_s\pi}C_l \\ 0 \\ \dfrac{4}{\mu_s\pi}C_{m_{\mathrm{ea}}} + c_1\alpha_0 \end{bmatrix}, \quad K = \begin{bmatrix} 0 & -1 & 0 & 0 \\ c_2^2 & 2\zeta_h c_2 & 0 & 0 \\ 0 & 0 & 0 & -1 \\ 0 & 0 & c_1 & \zeta_\alpha\left(\dfrac{2}{\bar{u}}\right)r_\alpha^2 \end{bmatrix} \tag{11}$$

The fluid dynamics equations are presented in nondimensional form and have the previously defined scales. The Euler equations for a moving airfoil in the flow of a perfect gas are[4]

$$\frac{\partial \hat{U}}{\partial t} + \frac{\partial \hat{E}(U)}{\partial \xi} + \frac{\partial \hat{F}(U)}{\partial \eta} = 0 \tag{12}$$

$$\hat{E} = (\xi_x\bar{E} + \xi_y\bar{F})/J, \qquad \hat{F} = (\eta_x\bar{E} + \eta_y\bar{F})/J \tag{13}$$

$$\hat{U} = U/J, \qquad J = \xi_x\eta_y - \xi_y\eta_x \tag{14}$$

$$U = \begin{bmatrix} \rho \\ \rho u \\ \rho v \\ E_t \end{bmatrix}, \quad \bar{E} = \begin{bmatrix} \rho(u - u_g) \\ \rho u(u - u_g) + p \\ \rho v(u - u_g) \\ E_t(u - u_g) + pu \end{bmatrix}$$

$$\bar{F} = \begin{bmatrix} \rho(v - v_g) \\ \rho u(v - v_g) \\ \rho v(v - v_g) + p \\ E_t(v - v_g) + pv \end{bmatrix} \tag{15}$$

The grid speeds, u_g and v_g, and the dynamic airfoil boundary conditions are developed as follows. The vector r_0 is a position vector from the origin of the inertial reference frame to the elastic axis origin, expressed in terms of the vertical displacement as $r_0 = h\hat{j}$. The vector r_b is a vector from the inertial origin to a position on the body. The local position vector $r_b - r_0$ is

$$r_b - r_0 = \bar{x}\hat{e}_1 + \bar{y}\hat{e}_2 = x_{\mathrm{in}}\hat{i} + (y_{\mathrm{in}} - h)\hat{j} \tag{16}$$

where $\bar{x} = x - x_{\mathrm{ea}}$ and $\bar{y} = y - y_{\mathrm{ea}}$, and

$$\begin{aligned} x_{\mathrm{in}} &= \bar{x}\cos\alpha + \bar{y}\sin\alpha \\ y_{\mathrm{in}} &= -\bar{x}\sin\alpha + \bar{y}\cos\alpha + h \end{aligned} \tag{17}$$

The inertial velocity of a point on the body in the inertial reference frame is

$$U_b = \Omega \times (r_b - r_0) + \dot{r}_0 = -\Omega(y_{\mathrm{in}} - h)\hat{i} + (\Omega x_{\mathrm{in}} + \dot{h})\hat{j} \tag{18}$$

The pitch rate vector, Ω, is related to α by $\Omega = \Omega\hat{k} = -\dot{\alpha}\hat{k}$. For all grid points, the grid speeds, u_g and v_g, in the inertial reference frame satisfy a relationship similar to Eq. (18):

$$u_g = -\Omega(y_{\mathrm{in}} - h), \qquad v_g = \Omega x_{\mathrm{in}} + \dot{h} \tag{19}$$

The far-field boundary conditions are written in a time-evolutionary form to maintain consistency between the time-dependent and time-independent algorithms. The inflow conditions, $U = U_\infty$, are written as

$$U^{n+1} = U^n - \Delta t\left[\frac{1}{\Delta t}(U^n - U_\infty)\right], \quad U_\infty = \begin{bmatrix} 1 \\ 1 \\ 0 \\ \dfrac{1}{\gamma(\gamma - 1)M_\infty^2} + \dfrac{1}{2} \end{bmatrix} \tag{20}$$

The outflow conditions are evolutionary forms of the conditions $\rho_x = 0$, $(\rho u)_x = 0$, $(\rho v)_x = 0$, and a specification of total energy. The airfoil surface boundary conditions consist of flow tangency for a moving airfoil, vanishing normal pressure gradient, $(\partial p/\partial n) = 0$, and the adiabatic wall condition.

Method of Solution

This section describes discretization of the governing equations and the boundary conditions. When the governing equations [Eq. (12)] are discretized, the fluxes are modified to enhance shock capturing. The modification follows the approach of the Harten-Yee upwind TVD scheme.[10] Equation (12) is split into two operators, one for each coordinate direction:

$$L_\eta\hat{U}^n_{i,j} = \hat{U}^*_{i,j} = \hat{U}^n_{i,j} - \Delta t(\hat{F}^n_{i,j+1/2} - \hat{F}^n_{i,j-1/2}) \tag{21}$$

$$L_\xi\hat{U}^*_{i,j} = \hat{U}^{**}_{i,j} = \hat{U}^*_{i,j} - \Delta t(\hat{E}^*_{i+1/2,j} - \hat{E}^*_{i-1/2,j}) \tag{22}$$

The fluxes $\hat{E}$ and $\hat{F}$ are modified to implement the second-order upwind TVD formulation. Details are provided in Ref. 7. The flowfield solution is advanced forward in time by Δt, with first-order temporal accuracy by

$$\hat{U}^{n+1}_{i,j} = L_\xi L_\eta \hat{U}^n_{i,j} \tag{23}$$

Time integration of the PAPA model involves a loose coupling of Eq. (23) with Eq. (8). The values of C_l and C_m obtained from the aerodynamic analysis are used when advancing the structural model [Eq. (8)] forward in time with a fourth-order Runge–Kutta algorithm.[12] The integration procedure maintains a Δt lag between the flowfield variables and the structural variables, and is first-order accurate in time and second-order accurate in space.

The grid topology for the current study is an O-grid. The subscripts i and j denote cell-center indices around the airfoil, ξ, and normal to the airfoil, η, respectively, and range from 1 to I and J, respectively. For the i index, four cells are physically redundant, providing an overlap of the computational domain along a virtual cut in the physical domain. The cut is directed upstream, starting from the leading edge of the airfoil. The far-field boundary is specified to be circular with a radius of $R_{\max}$; the grid is centered about the origin of the airfoil-fixed reference system. In the normal-coordinate direction at the airfoil surface, cell centers are positioned a distance Δ_{wall} apart.

Table 1 Specification of grids G1 and G2

Grid	Airfoil	I	J	$R_{\max}$	Δ_{wall}
G1	NACA 64A006	104	31	10	0.015
G2	NACA 64A006	104	15	10	0.015

Two grids, G1 and G2, are used for all calculations, and are defined in Table 1.

The outflow equations are placed in discrete form as follows:

$$f_{i,j}^{n+1} = f_{i,j}^{n} - \Delta t \left\{ \frac{u_{i,j}^{n}}{2} [\xi_{x_{i,j}} \Delta f_{i,j}^{n} + \eta_{x_{i,j}} (3 f_{i,j}^{n} - 4 f_{i,j-1}^{n} + f_{i,j-2}^{n})] \right\} \tag{24}$$

$$E_{t_{i,j}}^{n+1} = E_{t_{i,j}}^{n} - \Delta t \left[\frac{1}{\Delta t} (E_{t_{i,j}}^{n} - E_{t_\infty}) \right] \tag{25}$$

where f is either ρ, ρu, or ρv, and the form of Δf is

$$\Delta f_{i,j}^{n} = \begin{cases} 3 f_{i,j}^{n} - 4 f_{i-1,j}^{n} + f_{i-2,j}^{n} & \text{for} \quad \xi_{x_{i,j}} \geq 0 \\ -3 f_{i,j}^{n} + 4 f_{i+1,j}^{n} - f_{i+2,j}^{n} & \text{for} \ \xi_{x_{i,j}} < 0 \end{cases} \tag{26}$$

The pressure and temperature conditions at the airfoil surface are placed in discrete form using standard three-point formulas.

Equilibrium points are computed in addition to unsteady, limit-cycle solutions. Equilibrium solutions are obtained by assuming $\hat{U}_{i,j}^{n+1} = \hat{U}_{i,j}^{n}$, leading to the following system of nonlinear, algebraic equations:

$$\boldsymbol{F}_k \equiv \frac{\boldsymbol{U}_{i,j}^{n+1} - \boldsymbol{U}_{i,j}^{n}}{\Delta t} = (L_\xi L_\eta \hat{U}_{i,j}^{n} - \hat{U}_{i,j}^{n}) \frac{J_{i,j}}{\Delta t} = 0 \tag{27}$$

where k maps (i, j) into a single value, is an ordering for the linear system, and affects the bandwidth of the matrix. F is defined to be the set of all F_k. The system that models the fluid–structure interaction is composed of Eqs. (8) and (27), and is put into the form of Eq. (1) with

$$\boldsymbol{Y} = \begin{bmatrix} \boldsymbol{U} \\ \boldsymbol{S} \end{bmatrix}, \qquad \boldsymbol{G} = \begin{bmatrix} \boldsymbol{F} \\ \mathcal{H} \end{bmatrix} \tag{28}$$

Equilibrium solutions of Eq. (1) satisfy $\boldsymbol{G}(Y, \tilde{\lambda}) = 0$ and are calculated with Newton's method, adopting the convention $\tilde{\lambda} = \bar{u}$. One Newton iterate is obtained by solving the linear system:

$$\boldsymbol{G}_Y^\nu \Delta Y = -\boldsymbol{G}^\nu, \qquad \Delta Y = Y^{\nu+1} - Y^\nu \tag{29}$$

where the Jacobian matrix is given by

$$\boldsymbol{G}_Y = \begin{bmatrix} \boldsymbol{F}_U & \boldsymbol{F}_S \\ \mathcal{H}_U & \mathcal{H}_S \end{bmatrix} \tag{30}$$

The structure of $\boldsymbol{G}_Y$ for an O-grid topology and the chosen collocation strategy is a bordered, banded matrix. The matrix $\boldsymbol{F}_U$ is bordered and banded, with bordered elements corresponding to the grid cut locations; $\boldsymbol{F}_S$ and $\mathcal{H}_U$ have column and row dimensions of 4, respectively, and are treated as full arrays; $\mathcal{H}_S$ is a full, four-by-four matrix. Newton iterates are repeated until convergence is obtained (or divergence is established) measured by the residual L_2 norm:

$$\|G\|_2 \equiv \sqrt{\sum_{k=1}^{n} G_k^2(Y, \tilde{\lambda})} \tag{31}$$

It should be noted that analytical determination of the Jacobian elements of $\boldsymbol{G}_Y$ is quite difficult. To circumvent this problem and to allow the developed software to compute solutions for a wide variety of engineering problems, the Jacobian elements are computed numerically using second-order-accurate finite differences.[7,9]

At a Hopf-point, a steady-state solution transitions to an oscillatory solution with zero amplitude.[13] The Hopf-point solution is specified to be an oscillatory perturbation to an equilibrium solution ($\boldsymbol{Y}^0$), $\boldsymbol{Y} = \boldsymbol{Y}^0 + \varepsilon \boldsymbol{P} e^{\beta t}$, where ε is a vanishingly small parameter and $\boldsymbol{P}$ is a coefficient vector. Using the assumed form of the solution and a Taylor-series expansion for $\boldsymbol{G}(Y, \tilde{\lambda})$ yields

$$\boldsymbol{G}(Y, \tilde{\lambda}) = \boldsymbol{G}^0 + \varepsilon e^{\beta t} \boldsymbol{G}_Y^0 \boldsymbol{P} + \mathcal{O}(\varepsilon^2) \tag{32}$$

where $\boldsymbol{G}^0 \equiv \boldsymbol{G}(Y^0, \tilde{\lambda})$ and $\boldsymbol{G}_Y^0 \equiv \boldsymbol{G}_Y(Y^0; \tilde{\lambda})$. With Eq. (32), Eq. (1) becomes $\boldsymbol{G}^0 = 0$ at $\mathcal{O}[1]$ and

$$\boldsymbol{G}_Y^0 \boldsymbol{P} = \beta \boldsymbol{P} \tag{33}$$

at $\mathcal{O}[\varepsilon]$. The latter equation is an eigenproblem for the matrix $\boldsymbol{G}_Y^0$. The coefficient vector $\boldsymbol{P}$ is the eigenvector related to the eigenvalue β and has the form $\boldsymbol{P} = \boldsymbol{P}_1 + i\boldsymbol{P}_2$. With the Hopf-point condition $\beta_\pm = \pm i\Theta$, Eq. (33) yields two equations relating the real and imaginary parts of P[13]:

$$\boldsymbol{G}_Y \boldsymbol{P}_1 + \Theta \boldsymbol{P}_2 = 0, \qquad \boldsymbol{G}_Y \boldsymbol{P}_2 - \Theta \boldsymbol{P}_1 = 0 \tag{34}$$

At a Hopf-point, $\boldsymbol{P}_1$ and $\boldsymbol{P}_2$ are constrained by

$$q^T \boldsymbol{P}_1 = 0, \qquad q^T \boldsymbol{P}_2 = 1 \tag{35}$$

where q is a constant vector.[13] Thus, Hopf-points satisfy an expanded system of equations written as $\mathcal{F}(\mathcal{X}) = 0$, where

$$\mathcal{F} = \begin{bmatrix} \boldsymbol{G}_Y \boldsymbol{P}_1 + \Theta \boldsymbol{P}_2 \\ q^T \boldsymbol{P}_1 \\ \boldsymbol{G} \\ \boldsymbol{G}_Y \boldsymbol{P}_2 - \Theta \boldsymbol{P}_1 \\ q^T \boldsymbol{P}_2 - 1 \end{bmatrix} = 0, \qquad \mathcal{X} = \begin{bmatrix} \boldsymbol{P}_1 \\ \tilde{\lambda} \\ \boldsymbol{Y} \\ \boldsymbol{P}_2 \\ \Theta \end{bmatrix} \tag{36}$$

In principle, the expanded system can be solved with Newton's method:

$$\mathcal{F}_{\mathcal{X}}^{\nu} \Delta \mathcal{X} = -\mathcal{F}^{\nu} \tag{37}$$

where the expanded Jacobian matrix, $\mathcal{F}_{\mathcal{X}}$, is given by

$$\mathcal{F}_{\mathcal{X}} = \begin{bmatrix} \boldsymbol{G}_Y & (\boldsymbol{G}_Y \boldsymbol{P}_1)_{\tilde{\lambda}} & (\boldsymbol{G}_Y \boldsymbol{P}_1)_Y & \Theta \boldsymbol{I} & \boldsymbol{P}_2 \\ q_T & 0 & 0 & 0 & 0 \\ 0 & \boldsymbol{G}_{\tilde{\lambda}} & \boldsymbol{G}_Y & 0 & 0 \\ -\Theta \boldsymbol{I} & (\boldsymbol{G}_Y \boldsymbol{P}_2)_{\tilde{\lambda}} & (\boldsymbol{G}_Y \boldsymbol{P}_2)_Y & \boldsymbol{G}_Y & -\boldsymbol{P}_1 \\ 0 & 0 & 0 & q^T & 0 \end{bmatrix} \tag{38}$$

$\mathcal{F}_{\mathcal{X}}$ is a $(12N + 2) \times (12N + 2)$ matrix based on the grid topology and collocation strategy adopted in this work, where N represents the number of grid points. Unfortunately, it is very impractical to solve Eq. (37) directly, i.e., with Gaussian elimination, because $\mathcal{F}_{\mathcal{X}}$ is not banded. Furthermore, block-matrix strategies based on the full form of $\mathcal{F}_{\mathcal{X}}$ are not practical either, owing to the bordered structure of $\boldsymbol{G}_Y$ and the consequential fullness of $\boldsymbol{G}_Y \boldsymbol{G}_Y$.[9]

An alternative approach to computing Hopf-bifurcation points has been developed by the authors.[8,9] The strategy of the approach is to simplify $\mathcal{F}_{\mathcal{X}}$ to greatly improve the efficiency of a block-matrix solution of Eq. (37). With $\mathcal{F}_{\mathcal{X}}$ simplified, the quasi-Newton method is characterized by, but not identical to, successive block underrelaxation, where the underrelaxation parameter is denoted by ω. The starting point for the direct method is to drop ΘI from $\mathcal{F}_{\mathcal{X}}$:

$$\left[\begin{array}{ccc|cc} \boldsymbol{G}_Y & (\boldsymbol{G}_Y\boldsymbol{P}_1)_{\tilde{\lambda}} & (\boldsymbol{G}_Y\boldsymbol{P}_1)_Y & 0 & \boldsymbol{P}_2 \\ q^T & 0 & 0 & 0 & 0 \\ 0 & \boldsymbol{G}_{\tilde{\lambda}} & \boldsymbol{G}_Y & 0 & 0 \\ \hline -\Theta \boldsymbol{I} & (\boldsymbol{G}_Y\boldsymbol{P}_2)_{\tilde{\lambda}} & (\boldsymbol{G}_Y\boldsymbol{P}_2)_Y & \boldsymbol{G}_Y & -\boldsymbol{P}_1 \\ 0 & 0 & 0 & q^T & 0 \end{array}\right] \Delta\mathcal{X} = -\begin{bmatrix} \boldsymbol{G}_Y\boldsymbol{P}_1 + \Theta\boldsymbol{P}_2 \\ q^T\boldsymbol{P}_1 \\ \boldsymbol{G} \\ \boldsymbol{G}_Y\boldsymbol{P}_2 - \Theta\boldsymbol{P}_1 \\ q^T\boldsymbol{P}_2 - 1 \end{bmatrix} \tag{39}$$

$$\mathcal{X}^{\nu+1} = \mathcal{X}^{\nu} + \omega\Delta\mathcal{X} \tag{40}$$

This simplification is sufficient to remove the necessity of manipulating $\boldsymbol{G}_Y\boldsymbol{G}_Y$ when solving $\mathcal{F}_{\mathcal{X}}$ in full, block-matrix form. The vertical and horizontal lines in the system operator highlight the closeness of the operator to a block-lower triangular matrix. However, in the final form of the Hopf-point algorithm, the four diagonal terms in $\Theta \boldsymbol{I}$ corresponding to the structural dynamics equations are kept to enhance the convergence properties of the method. Without these terms, convergence is adversely affected by the smallness of main-diagonal elements corresponding to the structural dynamics equations when the structural damping is light.

Computation of the Hopf-point for a symmetric airfoil is simplified for the special case $\alpha_0 = 0$, when $\bar{u}$ is the free parameter. Because $\boldsymbol{G}_{\tilde{\lambda}} = \boldsymbol{G}_{\bar{u}} = 0$, the third equation in system (37) decouples from the other four equations. This decoupling allows the system to be computed more efficiently by eliminating the third row and third column from the Newton's method problem. The approximate Newton's method is simplified with the same modification. The simplified approximate Newton's method is termed the four-equation Hopf-point algorithm, whereas the unsimplified form is termed the five-equation Hopf-point algorithm.

Regular points are computed in the neighborhood of a Hopf-point and used as initial approximations to the solution vector. The eigenvector components $\boldsymbol{P}_1$ and $\boldsymbol{P}_2$ are initialized by setting $\boldsymbol{P}_1 = \boldsymbol{P}_2 = 1/\sqrt{4(N-1)}$. The normalization vector q is formed by the relationship:

$$q = \boldsymbol{P}_2/\boldsymbol{P}_2^T\boldsymbol{P}_2 \tag{41}$$

which satisfies the second normalization condition $q^T\boldsymbol{P}_2 = 1$.

Results and Discussion

This section presents the results for a NACA 64A006 airfoil at transonic freestream Mach numbers with a pitch-and-plunge structural dynamics model. First, the time-accurate algorithm is validated through comparison with published, time-integration solutions. Next, the consistency between the time-integration analysis and the Hopf-bifurcation analysis is established. The computational requirements associated with time integration and Hopf-point computation are compared. Finally, flutter boundaries for variations in freestream Mach number, M_∞, static pretwist, α_0, and pitch and plunge damping, respectively, ζ_h, ζ_α, are presented.

Table 2 Values of PAPA model parameters

Model	x_{cg}	x_α	$\zeta_h = \zeta_\alpha$	ω_h/ω_α	r_α^2	μ_s	M_∞	α_0
MP1	0.5	−0.2	0.0	0.3434	0.29	10	0.87	0
MP2	0.375	−0.25	0.5	0.2	0.25	125	0.85	0

Two sets of structural and aerodynamic model parameters are assumed throughout this work. These are denoted by MP1 and MP2. The parameter values corresponding to each set are provided in Table 2; comparison with numerical results reported by Ref. 4 motivates set MP1, whereas Ref. 3 guides the choice of set MP2.

Parameters M_∞, α_0, ζ_h, and ζ_α for set MP2 are varied when computing flutter boundaries. Note that for all computations, $\zeta_h = \zeta\alpha$ is assumed.

Validation of Time-Integration Procedure

Validation of the time-accurate algorithm described here consists of comparison with solutions reported by Kousen and Bendiksen,[4] hereafter referred to as KB, and with solutions obtained using ENS3DAE, a Beam–Warming, Euler–Navier–Stokes algorithm for three-dimensional flows.[14] Parameter set MP1 is assumed for all three methods, and grid G1 is used for the solutions obtained with ENS3DAE and the current method. Results of a grid-sensitivity study and additional validation comparisons are presented elsewhere.[9]

With ENS3DAE, the PAPA model is modified to treat a rectangular, rigid wing. Grid G1 is used as the cross-sectional two-dimensional plane of the three-dimensional grid necessary for ENS3DAE. Two-dimensional flow is enforced by placing inviscid planes at the wing tips. The ENS3DAE solutions are computed with the Euler option of the code. Specific parameters used in the ENS3DAE simulations as well as detailed discussions of ENS3DAE are included in Ref. 15. The Kousen and Bendiksen grid is a C-grid topology with 96 × 16 points.

Figure 2 presents the time-integration results for all three methods. The reduced velocity associated with the flutter onset point, $\bar{u}^*$, is found to be 1.90 for the current method, 1.92 for ENS3DAE, and 1.96 for KB, obtained through curve fits of α_{LC} for each method. The Hopf-point locations predicted by the present method and ENS3DAE differ by less than 1%, even though the dissipation models are significantly different. The KB solutions show less than a 3% difference in the Hopf point, even though the grid and the dissipation model are very different. The good comparison between the Hopf-point estimated with the current method and with KB and ENS3DAE give confidence in the solutions of the current method.

Although the predictions of flutter onset are in excellent agreement, which is of particular significance to this work, the oscillation amplitude for angle-of-attack, α_{LC}, differs between the three methods when $\bar{u} > \bar{u}^*$. The relatively large differences in α_{LC} between the current method and ENS3DAE can arise from noteworthy differences in the numerical dissipation models and the time steps used in the two algorithms.[9] However, we have not yet conducted grid, time-step, or dissipation–parameter sensitivity studies to evaluate the accuracy of either

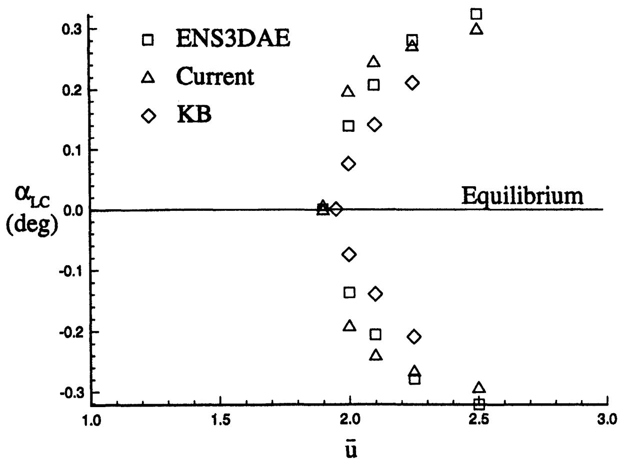

Fig. 2 Comparison of time-integration methods: $M_\infty = 0.87$, $\alpha_0 = 0$, and $\zeta_\alpha = \zeta_h = 0$.

method in simulating limit-cycle oscillation (LCO). It should be noted that superior comparisons of unsteady solutions, obtained with both methods, have been found for cases of driven pitch and driven plunge.[15] Obviously, the self-excited nature of LCO exacerbates deficiencies in either or both time-integration algorithms.

Validation of Hopf-Bifurcation Analysis

The consistency of the Hopf-bifurcation analysis with time integration is established in this section in terms of the predicted value of the flutter onset speed. Parameter set MP2 is assumed for this validation study, as well as grid G1.

The Hopf-point computation follows two steps. First, an equilibrium solution is computed for a particular reduced velocity, $\bar{u}$, using Newton's method. Next, the Hopf-point is computed directly with the Hopf-point algorithm. The Hopf-point solutions are considered converged when the maximum of the L_2 residual norms of $\mathcal{F}_1 - \mathcal{F}_5$ is less than 10^{-5}.

For parameter set MP2, the Hopf-point is found to be located at $\tilde{\lambda}^* = \bar{u}^* = 10.2838$ and $\Theta = 0.1029$. The Hopf-point is obtained after approximately 100 iterations with $\bar{u}$ initialized to 8 and the underrelaxation parameter, ω, set to 0.1. Small ω values are necessary for this Mach number when initializing P_1 and P_2 as previously described.

Time integration of the PAPA model is performed to validate the stability properties predicted by the Hopf-point algorithm. The time-accurate solution is obtained by computing an equilibrium solution at, typically, $\alpha = 0.1$ deg (0.0017 rads) and then releasing both the pitch and plunge axes. For stable equilibrium points, the angle of attack asymptotes to an equilibrium value of zero. Different values of $\bar{u}$ between 9 and 14 are considered; tabulated results are provided in Table 3. With $\bar{u} = 9$, the equilibrium solution ($\alpha = 0$ deg) is stable and the time-oscillatory solution decays to the equilibrium state over several hundred time units.[9] The same behavior is observed, although with a slower decay rate, when $\bar{u} = 10.25$. At $\bar{u} = 10.29$, slightly greater than the value of $\bar{u}$ predicted by the Hopf-point analysis, the equilibrium state is unstable and a small-amplitude limit cycle develops with $\alpha_{\text{LC}} = \pm 0.01185$ deg (0.00002067 rads). Thus, time integration brackets flutter onset between 10.25 and 10.29, thereby being consistent with the Hopf-bifurcation analysis to within a maximum possible difference of 0.33%.

The time histories of α and h for $\bar{u} = 11$ are presented in Fig. 3. For both variables, the oscillations are seen to grow in amplitude with time; α_{LC} achieves peak values of ± 0.2269 deg (0.003960 rads). The solution takes approximately 2000 time units to develop a repeatable limit cycle. Limit-cycle behavior is also obtained for $\bar{u} = 14$, with $\alpha_{\text{LC}} = \pm 1.256$ deg (0.021930 rads). The evolving character of the limit cycle with increasing $\bar{u}$ is shown in Fig. 4 as a series of phase-space representations of $\alpha(t)$ vs $h(t)$ (at least two complete cycles are shown for each value of $\bar{u}$ to demonstrate limit-cycle behavior). In the phase space shown, the cycles emerge with an elliptical shape, becoming somewhat asymmetric about the nominal major axis at $\bar{u} = 14$. Values of α_{LC} are plotted against $\bar{u}$ in Fig. 5 for all values of the reduced velocity examined.

Near the Hopf-point, the period of oscillation, T, can be estimated by the relationship $T = (2\pi/\Theta)$.[11] For the Hopf-point directly computed with the four-equation analysis, $T = 61.06$. Observed periods of oscillation for LCO are also provided in Table 3. At $\bar{u} = 10.29$ (a point very close to the Hopf point), the LCO period is 61.11, in excellent agreement (<0.1%) with the period estimated by bifurcation analysis. Furthermore, the trend of increased T with increased $\bar{u}$ (beyond $\bar{u}^*$) is observed for all values of $\bar{u}$ near the Hopf-point, including $\bar{u} = 10.29$. This trend appears to reverse when $\bar{u}$ becomes sufficiently large.

Table 3 Peak angle of attack and period for LCO

$\bar{u}$	α_{LC}, deg	α_{LC}, rad	Period, T_H
10.2838 (Hopf-point)	Infinitesimal	Infinitesimal	61.06
10.29	0.001185	0.00002067	61.11
10.50	0.06846	0.001195	61.22
10.75	0.1294	0.002259	61.45
11.00	0.2269	0.003960	61.55
12.00	0.7702	0.01344	60.34
14.00	1.256	0.021930	57.39

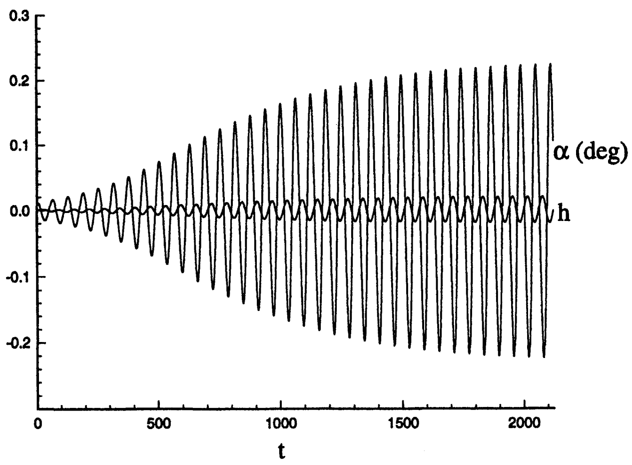

Fig. 3 Time integration of PAPA model: $\bar{u} = 11$ and $M_\infty = 0.85$.

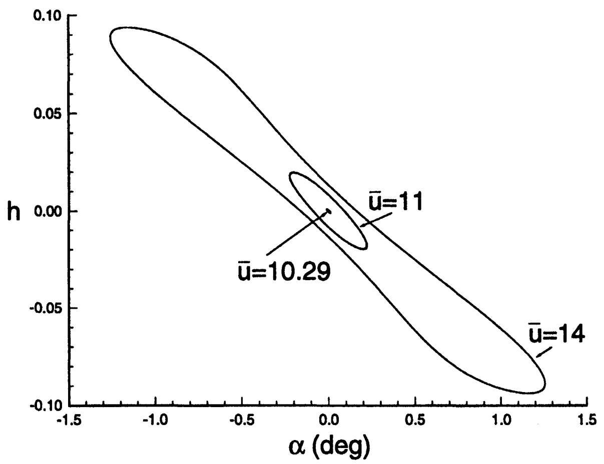

Fig. 4 Phase portraits of α vs h for selected values of $\bar{u}$ ($M_\infty = 0.85$).

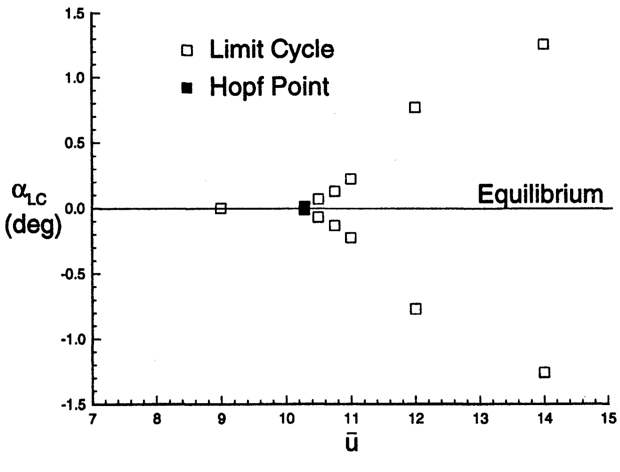

Fig. 5 Peak values of α during LCO at selected reduced velocities: $M_\infty = 0.85$, $\alpha_0 = 0$, and $\zeta_\alpha = \zeta_h = 0.5$.

Table 4 Computational requirements

Type	Grid	Memory, Mb	Time to covergence, h	Iterations
Equilibrium point	104 × 15	33	0.51	10
	104 × 31	117	3.53	10
Hopf-points	104 × 15	47	1.93	34
(four equations)	104 × 31	170	16.1	40 (estimated)
Hopf-points	104 × 15	67	13.2	35
(five equations)	104 × 31	232	93.7	40 (estimated)
Time integration	104 × 15	1.6	18	10^6 (estimated)
	104 × 31	2.9	56	10^6 (estimated)

Computational Requirements

The computational resources required to compute Hopf-point, regular-point, and unsteady solutions for the grids employed in this study are shown in Table 4. Computational times listed in the table are for a DEC 4620 workstation (using one 150-MHz central processor unit). Times to convergence for the 104 × 31 grid (G1) using four-equation and five-equation analyses are estimated, assuming 40 iterations. The number of time steps specified for the time-accurate solutions may or may not be sufficient to establish time-asymptotic behavior; a conservative estimate of 10^6 is chosen and reflects the large integration times necessary for states near Hopf-points. Table 4 documents the additional time, approximately eightfold, required to compute a Hopf-point with the five-equation algorithm. This increase in work is primarily associated with computing $(\boldsymbol{G}_Y\boldsymbol{P}_1)_Y$ and $(\boldsymbol{G}_Y\boldsymbol{P}_2)_Y$. Opportunities exist for more efficient computation of these matrices, through improved programming of the computational procedure for $\boldsymbol{G}$, which the authors are currently exploring.

NACA 64A006 Flutter Boundaries

A flutter boundary is modeled as a collection of Hopf-bifurcation points for different values of a specified free parameter. Three kinds of flutter boundaries are computed, each in terms of a different free parameter: freestream Mach number, pitch and plunge damping, and static pretwist. The flutter boundaries for Mach number and pitch and plunge damping are computed with the four-equation algorithm ($\alpha_0 = 0$ deg), whereas the flutter boundary for static pretwist requires the five-equation algorithm. The computation of these boundaries employs the grid described in the analysis section, and the values of the structural parameters defined in the previous section.

Figure 6 depicts the flutter boundary for M_∞ with $\alpha = \alpha_0 = 0$ deg and two different values of the pitch and plunge damping: 0.0 and 0.5. Figure 7 presents the same flutter boundaries in terms of Θ. The Hopf-point at $M_\infty = 0.85$, previously described, is used as the initial approximation for the solutions at neighboring values of M_∞. Each additional point on the flutter boundary is computed starting from the previous solution, including $\boldsymbol{P}_1$, $\boldsymbol{P}_2$, and Θ. Additional solution points require approximately 20 iterations each (with $\omega = 0.5$), representing a factor of 5 improvement over the number of iterations required to compute the initial solution at $M_\infty = 0.85$. The flutter boundary for no structural damping ($\zeta_h = \zeta_\alpha = 0$), composed of 18 Hopf-points, is computed in less than 24 h on a DEC 4620 workstation (using one processor).

Time-accurate solutions near the Mach flutter boundary are computed with the current time-integration method to verify a change in stability properties across the boundary. These calculations are performed with structural damping ($\zeta_h = \zeta_\alpha = 0.5$) near the flutter point at $M_\infty = 0.85$, where the flutter boundary is observed to abruptly increase in slope. Four time-accurate cases are considered: $\bar{u} = 9$ and 11 with $M_\infty = 0.85$ and $M_\infty = 0.845$ and 0.855 with $\bar{u} = 11$. The initial states for these time-accurate calculations are equilibrium solutions for the corresponding values of $\bar{u}$ and M_∞. As shown in Fig. 6, for the equilibrium states above ($\bar{u} > \bar{u}^*$), the flutter boundary are unstable, and the transition to unsteady solutions are marked by limit-cycle oscillation, whereas for the equilibrium states below ($\bar{u} < \bar{u}^*$), the flutter boundary are stable. The results of time integration validate the change in stability properties predicted by the Hopf-bifurcation analysis and also verify the observed rapid rise in $\bar{u}^*$ near $M_\infty = 0.85$.

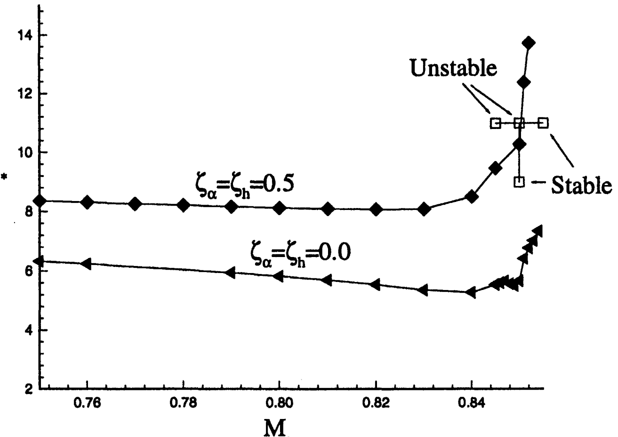

Fig. 6 Flutter boundaries for freestream Mach number with $\alpha_0 = 0$ (initial states for time integration marked with □; Hopf-points marked with filled symbols).

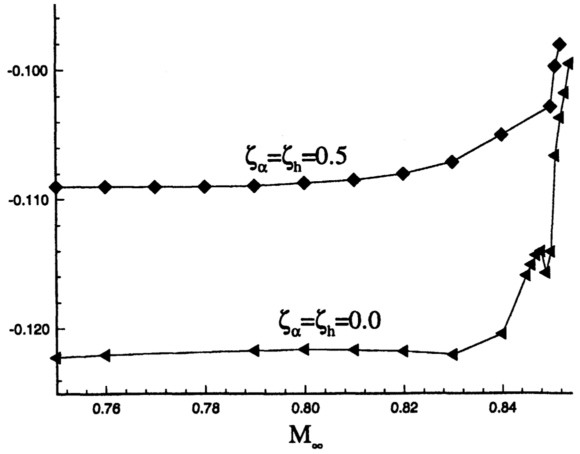

Fig. 7 Critical frequency vs freestream Mach number with $\alpha_0 = 0$.

For the case of no structural damping, Θ^* experiences an abrupt drop (1.5%) as the freestream Mach number is increased from 0.848 to 0.849. As seen in Fig. 7, this event occurs just prior to the abrupt rise in both $\bar{u}^*$ and Θ^*. The available data are insufficient to explain this behavior, but suggests two possible contributing factors: 1) anomalous behavior arising from grid coarseness, and 2) a switching of critical eigenvalue pairs, with different values of Θ, between $M_\infty = 0.848$ and 0.849. In examination of the latter, we have not been successful in smoothly tracing the progress of pairs across the

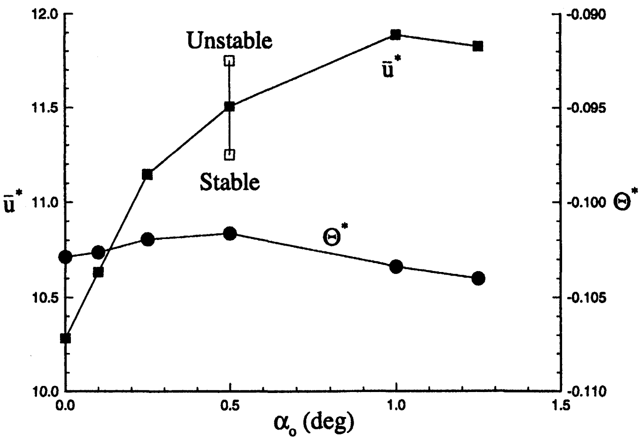

Fig. 8 Flutter boundary for static pretwist with $M_\infty = 0.85$ and $\zeta_\alpha = \zeta_h = 0.5$ (initial states for time integration marked with □; Hopf-points marked with filled symbols).

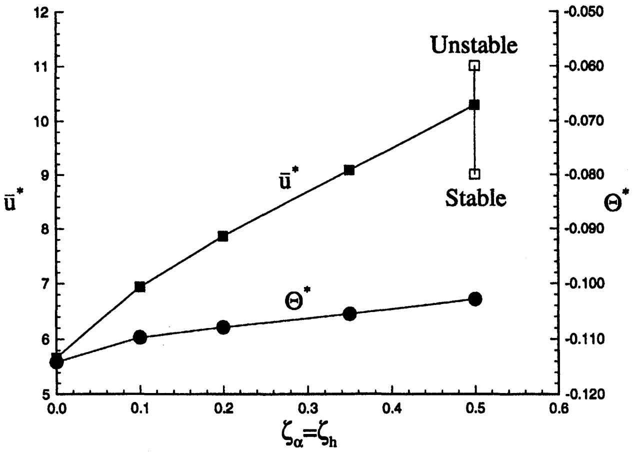

Fig. 9 Flutter boundary for pitch and plunge damping with $M_\infty = 0.85$ and $\alpha_0 = 0$ (initial states for time integration marked with □; Hopf-points marked with filled symbols).

switching region. To reproduce this detailed change in behavior of the flutter boundary near $M_\infty = 0.85$ with time integration would be extremely demanding computationally, because very precise estimates of flutter-point location would be required.

The flutter boundary for static pretwist, α_0, shown in Fig. 8, is represented by critical $\bar{u}$ and Θ. The computation of this flutter boundary verifies the ability of the five-equation analysis to obtain flutter solutions for nonzero angles of attack. Each point on the flutter boundary takes approximately 20 iterations to converge, starting from the known solution at $\alpha_0 = 0$ deg.

Stability in the neighborhood of the flutter boundary is evaluated through time integration using initial equilibrium states at $\bar{u} = 11.25$ and 11.75 with $\alpha_0 = 0.5$ deg. As shown in Fig. 8, the equilibrium state above the flutter boundary is unstable, while the equilibrium state below the flutter boundary is stable. This observed change in stability is consistent with the location of the flutter point directly computed with the five-equation algorithm.

Figure 9 depicts the flutter boundary as pitch damping, ζ_α, and plunge damping, ζ_h, values are varied simultaneously. It is observed that to a high degree, $\bar{u}^*$ varies linearly with $\zeta_\alpha = \zeta_h$ over the range 0.2–0.75.

Accuracy of Flutter Onset Predictions

A quantification of the accuracy of the reported values of $\bar{u}^*$ requires an analysis of the sensitivity of $\bar{u}^*$ to variation of grid parameters. It has already been shown that the Hopf-bifurcation analysis is highly accurate in providing $\bar{u}^*$ for a specified grid (typically within 1% compared to time integration). However, sizeable discretization errors can arise that affect absolute accuracy with the relatively coarse grids employed in this study, a current limitation of the fully implicit method. Morton has performed sensitivity analyses for both the computation of equilibrium-point and Hopf-point solutions of the Euler equations.[9] Using a grid of similar structure to grid G1 (but for a thicker NACA 0012 airfoil with $\Delta_{\text{wall}} = 0.005$), Morton observed an error of about 20% in C_l through systematic grid refinement for $M_\infty = 0.8$ and $\alpha = 1.25$ deg (0.0218 rads). For the same flow conditions, approximately a 25% error in C_l was found for a grid similar to grid $G2$, i.e., J decreased to about 15, but with $\Delta_{\text{wall}} = 0.005$. In a separate study involving Hopf-point computations, Morton observed that a 4% error in $\bar{u}^*$ is sustained when coarsening Δ_{wall} from 0.005 to 0.015. Thus, values of $\bar{u}^*$ could be in error by as much as 25–30%, assuming equivalent levels of sensitivity between $\bar{u}^*$ and C_l.

Conclusions

A validated method of directly computing the flutter onset point of a pitch-and-plunge airfoil is presented. This is the first direct calculation of flutter onset for an airfoil in the transonic regime with the Euler equations. The direct method is shown to be precise and efficient. Precision, for a specified set of model and grid parameters, is demonstrated in two ways. First, the direct method computes the flutter point without bracketing. Second, the direct method yields results entirely consistent with the current time-integration method. The flutter onset speed predicted by the current time-integration method is also found to be in excellent agreement with the results of two independent, time-integration methods. Thus, the level of accuracy of the Hopf-point analysis is consistent with that obtainable using other modern methods as applied to similar grids. Efficiency of the direct method is demonstrated by computing a flutter boundary for $0.75 \leq M_\infty \leq 0.854$ (composed of 18 flutter points) in 24 h on a workstation. Flutter boundaries associated with changes in structural parameters are also computed, further showing the ability of the method to explore thoroughly and efficiently the solution space of a pitch-and-plunge airfoil model.

To enhance the efficiency of the direct method when applied to the computation of flutter boundaries, it is recommended that a continuation methodology (such as pseudo-arc-length continuation) be added to the flutter analysis procedures described herein. Continuation would provide an efficient and automated approach to the computation of points on flutter boundaries, especially those boundaries that exhibit great sensitivity to variation of the free parameter, and would allow boundaries with folds to be traced.

Although the aerodynamic model incorporates the Euler equations for the current study, the method is not limited to this equation set. Addition of viscous terms is straightforward because of the numerical calculation of Jacobian elements. Implementing the Navier–Stokes equations in the PAPA model is recommended for future research to document the change in the flutter boundary with shock-wave boundary-layer interaction. Also, incorporating a nonlinear structural model capable of simulating structural freeplay or preload is recommended as future research, because the literature shows significant movement of the flutter point with small structural nonlinearities.

References

[1]Edwards, J. W., and Thomas, J. L., "Computational Methods for Unsteady Transonic Flows," AIAA Paper 87-0107, Jan. 1987.

[2]Edwards, J. W., and Malone, J. B., "Current Status of Computational Methods for Transonic Unsteady Aerodynamics and Aeroelastic Applications," NASA TM-104191, Jan. 1992.

[3]Wu, J., Sankar, L. N., and Kaza, K. R. V., "Technique for the Prediction of Airfoil Flutter Characteristics in Separated Flow," *Journal of Aircraft*, Vol. 26, No. 2, 1989, pp. 168–177.

[4]Kousen, K. A., and Bendiksen, O. O., "Nonlinear Aspects of the

Transonic Aeroelastic Stability Problem,'' AIAA Paper 88-2306, April 1988.

[5]Hui, W. H., and Tobak, M., "Bifurcation Analysis of Aircraft Pitching Motions About Large Mean Angles of Attack,'' *Journal of Guidance, Control, and Dynamics*, Vol. 7, No. 1, 1984, pp. 113–122.

[6]Beran, P. S., and Lutton, M. J., "Hopf Bifurcation in Viscous Flows About Airfoils at Low Speeds,'' AIAA Paper 91-1807, June 1991.

[7]Morton, S. A., and Beran, P. S., "Nonlinear Analysis of Airfoil Flutter at Transonic Speeds,'' AIAA Paper 95-1905, June 1995.

[8]Morton, S. A., and Beran, P. S., "Hopf-Bifurcation Analysis of Airfoil Flutter at Transonic Speeds,'' AIAA Paper 96-0060, Jan. 1996.

[9]Morton, S. A., "Nonlinear Analysis of Airfoil Flutter at Transonic Speeds,'' Ph.D. Dissertation, U.S. Air Force Inst. of Technology, Wright–Patterson AFB, OH, May 1996.

[10]Yee, H. C., "A Class of High Resolution Explicit and Implicit Shock Capturing Methods,'' NASA TM-101088, Feb. 1989.

[11]Seydel, R., *From Equilibrium to Chaos: Practical Bifurcation and Stability Analysis*, Elsevier, New York, 1988.

[12]Press, W. H., Flannery, B. P., Teukolsky, S. A., and Vetterling, W. T., *Numerical Recipes, The Art of Scientific Computing*, Cambridge Univ. Press, New York, 1987.

[13]Griewank, A., and Reddien, G., "The Calculation of Hopf Points by a Direct Method,'' *IMA Journal of Numerical Analysis*, Vol. 3, No. 1, 1983, pp. 295–303.

[14]Smith, M. J., Schuster, D. M., Huttsell, L., and Buxton, B. J., "Development of an Euler/Navier-Stokes Aeroelastic Method for Three-Dimensional Vehicles with Multiple Flexible Surfaces,'' AIAA Paper 96-1513, April 1996.

[15]Buxton, B. J., "Comparison of Two Shock Capturing Methods for Calculation of Transonic Airfoil Flutter,'' M.S. Thesis, U.S. Air Force Inst. of Technology, Wright–Patterson AFB, OH, Dec. 1995.

Have Blue and the F-117A: Evolution of the "Stealth Fighter"

David C. Aronstein and Albert C. Piccirillo, ANSER

Have Blue and the F-117A: Evolution of the "Stealth Fighter" documents the history, observations, and lessons learned from the development and acquisition of the first very-low-observable combat aircraft. The book is a case study of the high-payoff, low-profile strike fighter development effort (code-named "Have Blue" and "Senior Trend"). Most of the material presented in the book was once highly classified information.

The book describes the clear vision, strong leadership and teamwork, rapid-response decision-making, and keen focus on achieving an operational capability that marked the project. Also discussed are potential applications of the strategies used in the project to today's acquisition environment.

1997, 305 pp, Softcover
ISBN 1-56347-245-7
List Price: $54.95
AIAA Member Price: $39.95
Source: 945

American Institute of Aeronautics and Astronautics
Publications Customer Service, 9 Jay Gould Ct., P.O. Box 753, Waldorf, MD 20604
Fax 301/843-0159; Phone 800/682-2422; E-mail aiaa@tasco1.com
8 am–5 pm Eastern Standard

CA and VA residents add applicable sales tax. For shipping and handling add $4.75 for 1–4 books (call for rates for higher quantities). All individual orders, including U.S., Canadian, and foreign, must be prepaid by personal or company check, traveler's check, international money order, or credit card (VISA, MasterCard, American Express, or Diners Club). All checks must be made payable to AIAA in U.S. dollars, drawn on a U.S. bank. Orders from libraries, corporations, government agencies, and university and college bookstores must be accompanied by an authorized purchase order. All other bookstore orders must be prepaid. Please allow 4 weeks for delivery. Prices are subject to change without notice. Returns in sellable condition will be accepted within 30 days. Sorry, we cannot accept returns of case studies, conference proceedings, sale items, or software (unless defective). Non-U.S. residents are responsible for payment of any taxes required by their government.